Transonic Flutter Dips of the AGARD 445.6 Wing

Bret K. Stanford*, Kevin E. Jacobson†
NASA Langley Research Center, Hampton, VA, 23681

The AGARD 445.6 configuration is the most popular validation test case for transonic flutter predictions, but the actual extent of truly nonlinear transonic flow for this case is unclear, due to the sparsity of the experimental data, and the thin profile of the wing. This work utilizes a combination of mesh adaptation and the linearized frequency-domain method to obtain high-quality viscous and inviscid flutter predictions; these solutions show a double flutter dip through the transonic Mach range driven by complex shock growth across the wing. A single experimental flutter point lies in this flutter dip area, which is not enough to assess the accuracy of these transonic flutter predictions. Modeling the boundary layer of the wind tunnel wall (as opposed to the commonly-assumed symmetry wall assumption) appears to have a large impact on the predicted flutter boundary, but true mesh convergence of this scenario is a challenge.

I. Introduction

There is currently a lack of experimental validation data for transonic aeroelastic flutter. Computational predictions struggle to accurately capture the transonic flutter dip, where flutter dynamic pressure q can experience a sharp drop with small changes in Mach number.[1–3] This dip may be driven by strong aerodynamic nonlinearities: shocks and flow separation; the latter of which causes particular difficulties for modern CFD solvers. Of the available experimental data sets, the AGARD 445.6 configuration[4] is, by far, the most widely cited and used, both historically and currently. A sampling of papers from just the last five years is found in Refs. 5-12.

The AGARD configuration was tested in the NASA Langley Transonic Dynamics Tunnel (TDT) in 1961,[13] and consists of a symmetric swept tapered wing, cantilevered to the sidewall of the tunnel. Flutter q is available (at 0° angle of attack, AoA) at Mach numbers of 0.5, 0.678, 0.901, 0.96, 1.072, and 1.141, though no other data (pressures, flow fields, etc.) exist. The data at Mach numbers of 0.96 and 1.072 are ostensibly within the transonic flutter dip, and are frequently used to benchmark and validate CFD-based flutter tools. However, as noted in Refs. 14 and 15, the airfoil used on the AGARD wing is symmetric and very thin. When tested at 0° AoA, the range of Mach numbers for which "mixed" nonlinear flow exists is a very narrow band around Mach 1.0, and does not include many of the Mach numbers for which experimental data are available. A linear aerodynamic tool, then, should be able to reproduce most of the available flutter data for the AGARD configuration, as demonstrated in Ref. 16. This test case, then, may not be a good CFD-based flutter validation case; the flutter dip evidenced in the data is largely driven by compressible flow.

Nonlinear flutter mechanisms do exist for the AGARD 445.6; however, and though little experimental data are available at these Mach numbers (above the 0.901 data point, but below the 1.072 point), it is still of interest to utilize CFD-based flutter methods to explore the physics here. The state-of-the-practice[17] for CFD-based flutter is to couple an unsteady Reynolds-averaged Navier-Stokes (RANS) solver to a modal representation of the structure, and repeatedly integrate this system out in time for increasing q, until an instability is noted. This method is cumbersome, expensive, and does not always provide enough insight into the driving flutter mechanism.

Two new tools, recently available to computational aeroelasticians, will be utilized here for a more efficient and insightful computation of the AGARD flutter boundary. The first is the linearized frequency-domain (LFD) method, recently implemented[18] within the stabilized finite-element (SFE)[19] version of the FUN3D

*Research Aerospace Engineer, Aeroelasticity Branch, bret.k.stanford@nasa.gov, AIAA Associate Fellow.
†Research Aerospace Engineer, Aeroelasticity Branch, AIAA Member.

solver.[20] LFD linearizes about a steady background flow via infinitesimal oscillatory perturbations of each mode shape, resulting in a complex valued set of generalized aerodynamic forces (GAFs). These GAFs may then be used to directly compute flutter in a $p-k$ eigen-equation,[21] and the aeroelastic flutter mode can finally be reconstructed. The second tool used here is a multiscale mesh adaptation scheme[22] that has recently been expanded to work along side the LFD-based flutter solver.[23] The mesh adaptation code reduces spatial interpolation error in the flow field based on the scalar Mach number flow field (either the steady background flow, or some form of the unsteady flow field).

These two tools provide a complete elimination of any temporal errors (as the flow solver operates in the frequency domain), and at least a minimization and quantification of the spatial discretization errors. Results will be provided in terms of the flutter q-vs-Mach curves for linear panel solutions, inviscid CFD solutions (Euler), and viscous CFD solutions (RANS), with a particular emphasis on Mach numbers close to Mach 1.0, for which no experimental data is available, but for which the transonic behavior will be most pronounced. Where possible, emphasis is placed on drawing a connection between the steady background flow, the GAFs, the eigenvalue migration trends (with increasing q), the final flutter point, and the unsteady flow field, for a deeper insight into the physics driving the instability.

II. AGARD 445.6 Wing

The AGARD configuration has a root chord of 22 in., a 30 in. span, a 45° quarter-chord sweep angle, and a taper ratio of 0.66. The wing consists of a symmetric NACA65A004 airfoil extruded from root to tip. There is some discrepancy in the original literature[4] about whether the wingtip is flat or rounded, and the original wind tunnel model is lost[a]. For most of the results in this work, a flat wingtip is used (this is the most common choice in the literature as well), though some results will show a comparison with a rounded wingtip. The trailing edge thickness is set here to zero, again lacking any documentation to the contrary.

The plate-like wing structure, clamped along a portion of the root, consists of a weakened orthotropic mahogany material with a nonuniform thickness distribution. The first four mode shapes are retained for aeroelastic analysis; the shapes themselves can be seen in Ref. 15, and the structural frequencies are 9.58, 38.16, 49.52, and 91.72 Hz. No structural damping is included in this work.

III. Numerical Tools

All CFD simulations are conducted in the SFE[19] flow path of the FUN3D solver.[20] Having computed the steady flow over the wing, the LFD solver[18] is used to compute the GAFs, which finally enables computation of the flutter q. Mesh adaptation mechanics are handled with a sketch-to-solution workflow,[24,25] specifically the *refine*[b] tool. The adaptations reduce spatial interpolation error in the flow field based on some multiscale metric[22] scalar field, Mach number in this work.

The overall workflow is summarized as follows:

1. An EGADS model[26] of the geometry is generated. *refine* uses this geometry to generate a coarse initial volume mesh (roughly $1{\cdot}10^4$ nodes), which is used for inviscid (Euler) mesh adaptation results. For RANS, a finer initial mesh is generated (roughly $1{\cdot}10^5$ nodes) with an initial boundary layer spacing via Spalding's law of the wall.[27]
2. A steady flow simulation is conducted with FUN3D/SFE.
3. A radial basis function tool is used to interpolate the four structural mode shapes onto the surface mesh.
4. Using 10 reduced frequencies between 0 and 2.0, the LFD solver computes the set of GAFs, via 40 complex-valued linear problems. A $p-k$ solver computes the flutter q.
5. Using the scalar Mach field from the steady flow solution, *refine* generates the next mesh, and the process returns to step 2.

Defining complexity as a continuous measure of the refinement (where the number of nodes in the mesh is roughly equal to double the complexity), a controller is implemented in the above workflow that doubles the

[a] Chwalowski, P., personal communication.

[b] Available via https://github.com/NASA/refine, last accessed June, 2021.

complexity every fourth cycle of adaptation. As noted above, the refinement mechanics are driven by the steady flow. More sophisticated schemes have been implemented in Ref. 23, where the mesh adaptation is driven by a series of unsteady snapshots reconstructed from the fluttering mode shape, but this idea is not used here. As such, steps 3 and 4 above do not actually impact the mesh mechanics in any way, and could be conducted as a post-processing step after the entire mesh adaptation process has completed.

It is also noted that, because results are computed at 0° AoA for this symmetric wing, a static aeroelastic solution can be omitted, substantially simplifying the workflow. Otherwise, an iterative link would have to be established between the flutter q, and the steady q used to compute the static aeroelastic result. Even with the trivial static aeroelastic solution of this configuration, there is another iterative relationship for the RANS simulations considered here, in that the Reynolds number used for the steady FUN3D/SFE analysis will depend on the flutter q, and vice-versa. This sort of matched-point analysis is ignored here, however, and the Reynolds number is simply derived from the experimental flutter q at each Mach number (and interpolated at Mach numbers not included in the experiment).

IV. Results

Flutter boundary results are shown in Fig. 1, in terms of the TDT experimental data,[4] inviscid Euler results, viscous RANS results, and linear results. These results use a geometry with a flat wingtip, and a symmetry plane boundary condition at the root. Linear results are computed via the subsonic and supersonic unsteady panel aerodynamic tools found in MSC/Nastran, with 32 equally-spaced spanwise boxes and 16 chordwise. The Euler and RANS results are taken from the final step of the mesh adaptation process, examples of which are seen in Fig. 2. The final Euler meshes contain roughly $3{\cdot}10^5$ nodes, and the final RANS meshes have roughly $3{\cdot}10^6$ nodes.

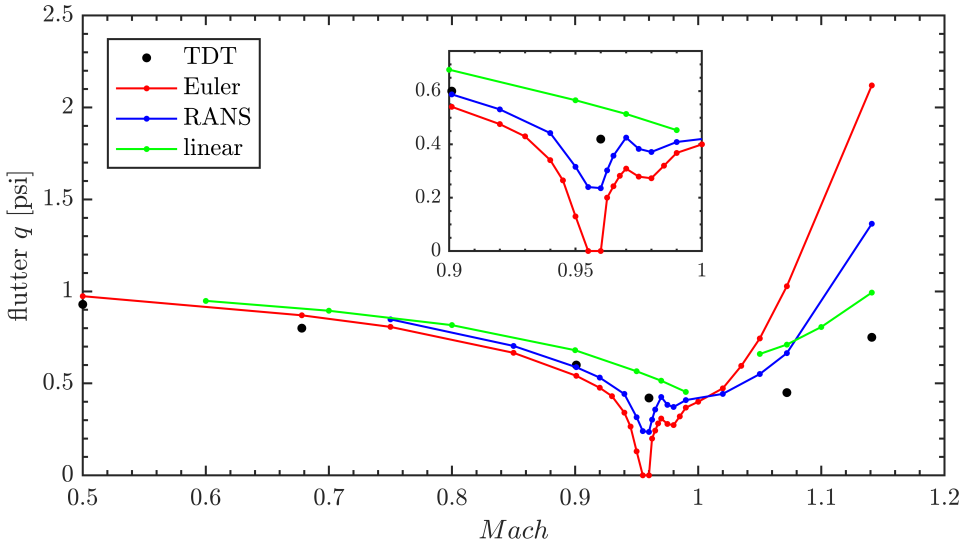

Figure 1: Flutter boundary measured in the TDT,[4] compared to linear, inviscid, and viscous predictions.

There are a number of interesting features in Fig 1:

1. The subsonic predictions (up to Mach 0.85) are all in good agreement with each other, and in good agreement with the TDT data. This is expected, given the weak nonlinearities for these flow conditions.
2. The supersonic predictions (above Mach 1.172) are all in very poor agreement with each other, and the TDT data. This has been previously observed in Ref. 15, and is not expected or understood, again given the weak nonlinearities for these flow conditions.
3. Between Mach 0.9 and Mach 1.0, there are substantial deviations in the Euler and RANS flutter boundaries, below the linear flutter predictions. There are two flutter dips: the first (and strongest) reaches a minimum at Mach 0.96. The Euler solver predicts a flutter q of 0 for this flow, while the RANS predicts a value of 0.236 psi. The second, weaker flutter dip occurs near Mach 0.98, and both

CFD solvers show a non-zero flutter q at this condition. A double flutter dip has been previously-observed in Ref. 9, though the first dip in that work (using Euler) does not reach 0 psi, and the second dip occurs at Mach 1.0. The mesh convergence in Fig. 2 would suggest that finer meshes are needed to obtain the 0-q flutter point, and that under-resolved meshes will return a nontrivial value.

4. The experimental data point at 0.96 clearly lies within the transonic region of the predicted flows, but both CFD solvers underpredict this point. There is too little data to know whether the solvers are mispredicting the location of the flutter dip, or the severity, or both.

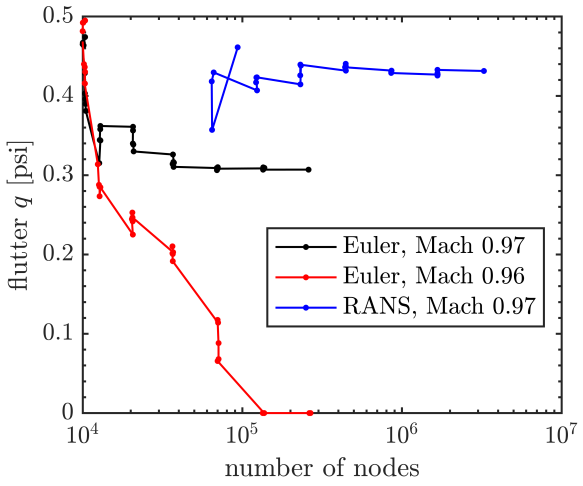

Figure 2: Flutter q convergence during the mesh adaptation process.

Eigenvalue migration plots (i.e., root locus plots) are shown in Fig. 3 for Mach numbers of 0.96 and 0.97, which clearly shows the mechanism by which the Euler solver returns a 0-q flutter point at the lower Mach value. If the complex-valued GAF matrix is noted as $\bar{\boldsymbol{A}}$, then the first 2×2 submatrix ($\bar{A}_{11}$, $\bar{A}_{21}$, $\bar{A}_{12}$, $\bar{A}_{22}$) is shown in Fig. 4. These GAFs are shown in the complex plane, where migrations along each curve are driven by increased reduced frequency, k. The reduced frequency at which flutter occurs is indicated in the figure, and this is a generally small value between 0.05 and 0.1 that qualifies the aerodynamics as quasisteady. It is also noted that the curves in Fig. 4 use a finer list of reduced frequencies than the basic ten values noted above, for plotting purposes only.

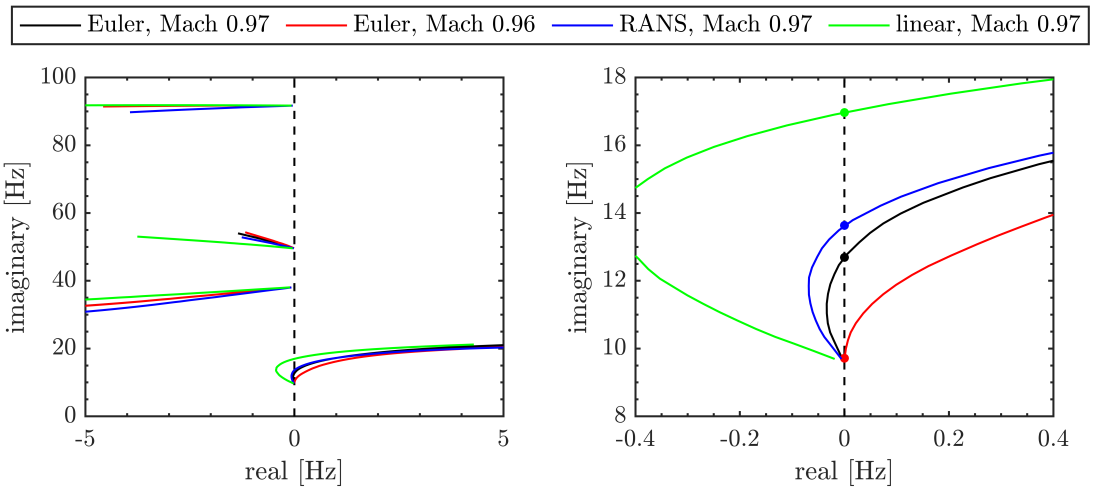

Figure 3: Root locus plots showing the aeroelastic eigenvalue migration (dots indicate the flutter point). Zoom-in of mode-1 flutter shown on right.

The four cases in Fig. 4 display expected variations, but the key difference that drives the transonic behavior is in the phase lag of the low-frequency $\bar{A}_{11}$ term. This term is shown in greater detail in Fig. 5, where the real and the imaginary parts of $\bar{A}_{11}$ are plotted vs k. For the 0-q Euler Mach 0.96 case, the imaginary part is slightly positive at flutter; for the other three cases in the figure, it is negative. A strong transonic dip will occur for values of $\bar{A}_{11}$ with a small imaginary part (i.e., a small phase lag between the structural motion and the aerodynamics); the dip will be weak for larger phase lags, as seen with the linear results for example.

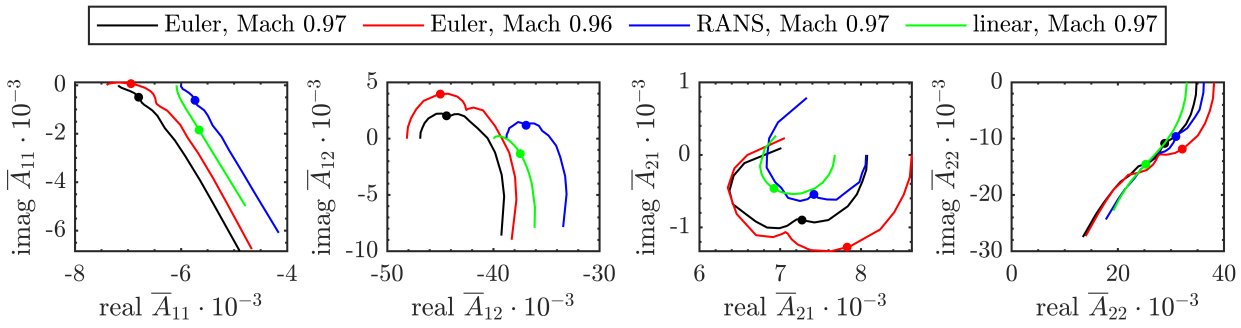

Figure 4: Migration of the complex-valued GAFs as a function of reduced frequency; dots indicate the flutter point.

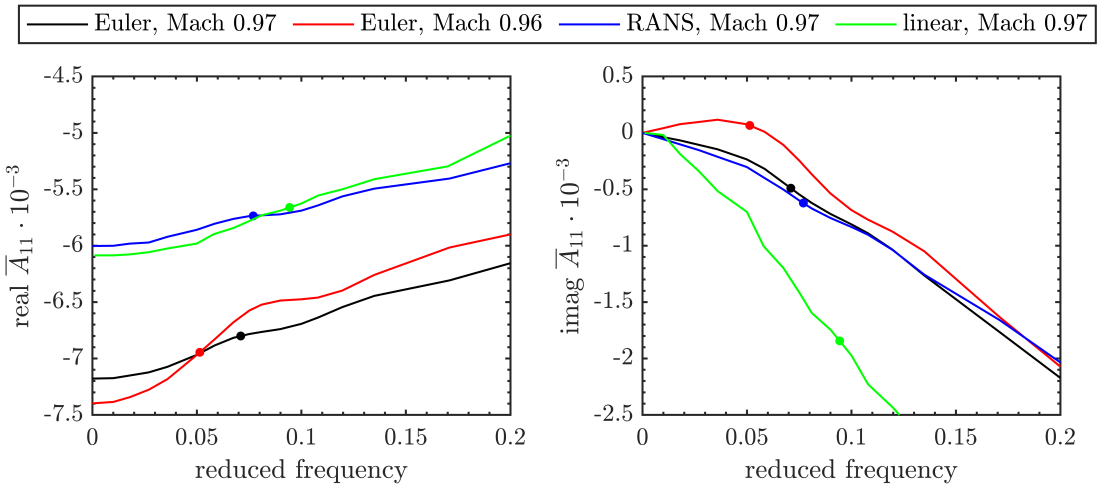

Figure 5: Migration of the complex-valued mode-1 GAF as a function of reduced frequency; dots indicate the flutter point.

The steady CFD surface pressures are shown in Fig. 6. These pressures generally agree well between Euler and RANs at each Mach value, with the inviscid results showing sharper shocks, as expected. Two shocks are present: one that starts at the trailing edge of the root and grows outboard with increased Mach number, and a second that starts at the leading edge of the wingtip, and grows inboard. At Mach 0.98, the former shock extends all the way to the wingtip, and this condition corresponds to the second flutter dip seen in Fig. 1. For lower Mach numbers than shown in Fig. 6, the small wingtip shock is still present, particularly for Euler flows. Furthermore, the peak Mach number inside this shock will continue to grow with increased mesh resolution. These trends are likely to be exacerbated in part by the flat wingtip geometry, whereas a rounded tip will mute these effects, as will be discussed below.

The complex-valued oscillatory pressures are shown in Fig. 7, in terms of the imaginary part of the pressures due to vibrations of the first bending mode at k=0.05, as these pressures (when integrated over mode 1, to form $\bar{A}_{11}$) have been shown to be the strongest driver for the transonic flutter dips. These oscillatory pressures, as computed by LFD, show strong variations across the shock, as would be expected. The contour axes have been clipped in Fig. 7 for ease of presentation, though in reality the peak LFD

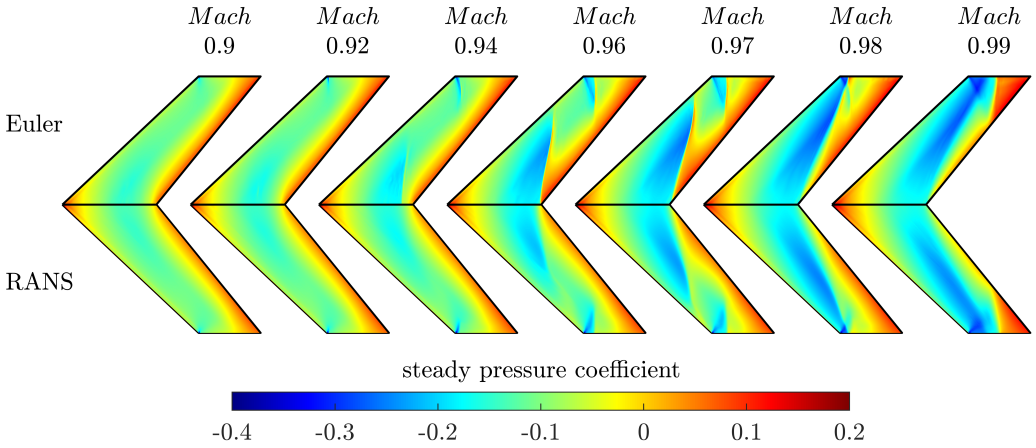

Figure 6: Steady transonic pressure coefficients computed by the Euler solver (upper row) and the RANS solver (lower row).

pressures before and after the shock are much larger than indicated in the figure. Again the two CFD results match well at each Mach number, with the exception of Mach 0.94, where the sharp fluctuations across the shock does not appear to be present for RANS. Despite this, as will be seen below, there is a supersonic bubble over the wing for the RANS result at Mach 0.94.

As noted above, integrating the result in Fig. 7 over the first bending mode will provide $\bar{A}_{11}$, and the magnitude and sign of this term will dictate the severity of the transonic flutter dip. The strength of $\bar{A}_{11}$ is not visually evident in Fig. 7; however, it is a result of the enormous fluctuations in these pressures near the shocks.

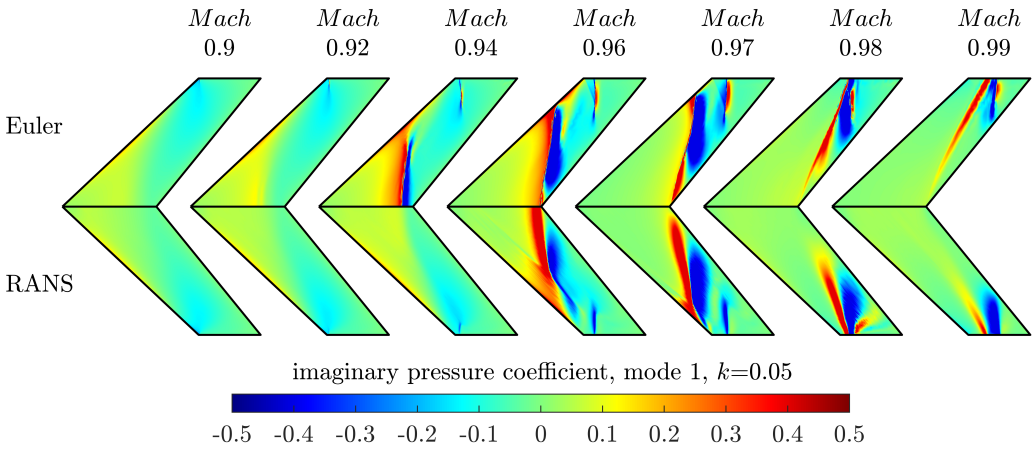

Figure 7: Imaginary pressure coefficients computed by the Euler solver (upper row) and the RANS solver (lower row) at $k = 0.05$.

Beyond the surface pressures in Fig. 6 and Fig. 7, additional indications of shock strength are shown in Fig. 8. For a subsonic freestream, this figure provides the volume of the supersonic bubble in the flow field, normalized by the volume of the wing itself. If this volume is small, transonic effects will be weak, and the flutter mechanism will be largely linear. A visualization of this bubble is shown in Figs. 9 and 10 for Mach 0.92 and 0.94. Similarly, Fig. 8 also shows the volume of the subsonic bubble within a supersonic freestream: again, if this volume is small, the flutter mechanism should be linear. The sum of the two curves will equal the total volume of the CFD mesh, and both curves approach very large values at the sonic condition.

For a subsonic freestream, the differences between RANS and Euler are minor, though the volume of the RANS supersonic bubble is slightly smaller for Mach numbers below 0.94. Both CFD models show a supersonic bubble larger than the wing itself, when the Mach number exceeds 0.95. For a supersonic freestream, the differences between the two CFD models are larger, with RANS consistently showing larger

regions of low-speed flow. This, however, is due to the volume of the boundary layer and the wake and is not necessarily a referendum on aeroelastic nonlinearities driving the transonic response.

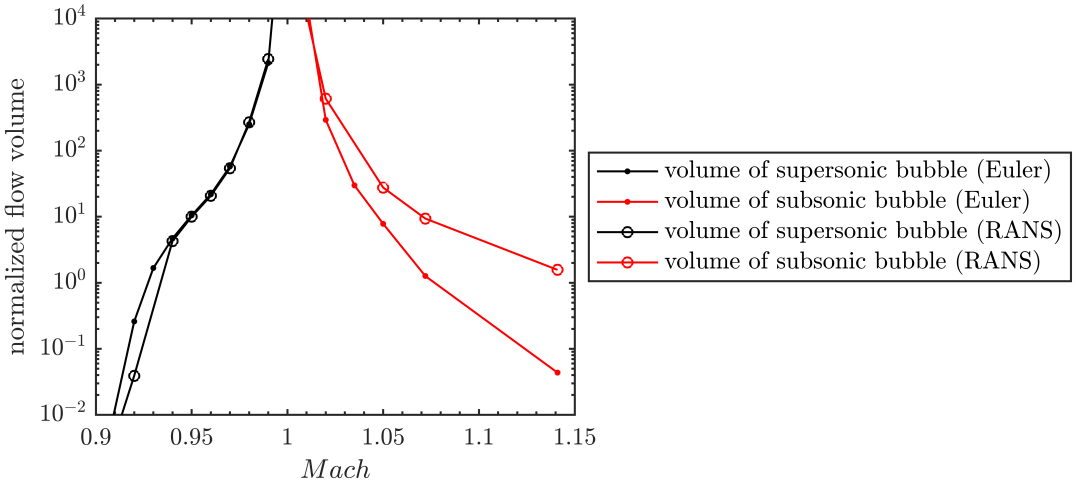

Figure 8: Black curves plot the volume of steady supersonic flow (normalized by the volume of the wing) when the freestream flow is subsonic. Red curves plot the normalized volume of steady subsonic flow when the freestream flow is supersonic.

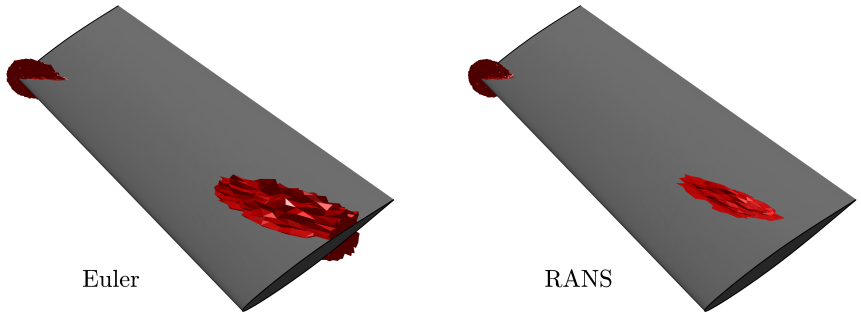

Figure 9: Sonic isosurface, when the freestream Mach is 0.92.

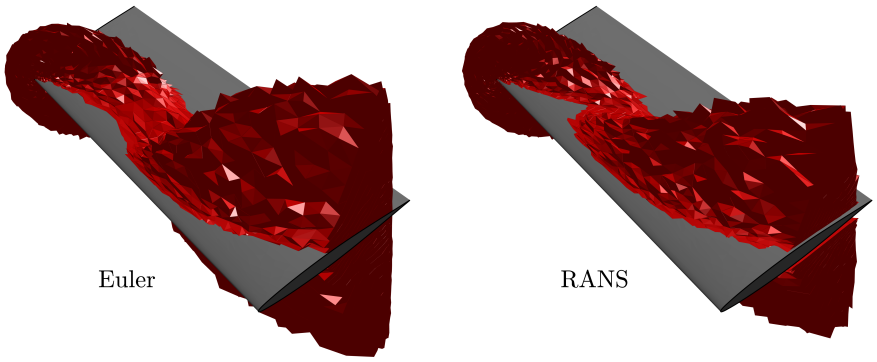

Figure 10: Sonic isosurface, when the freestream Mach is 0.94.

As noted above, the Euler solver predicts large local Mach numbers in the flow around the flat wingtip, and these values grow larger with increased mesh density. To understand the degree to which this behavior impacts the instability boundary, Figure 11 compares flutter results with a rounded wingtip, where results from the flat wingtip are repeated from Fig. 1. It can be seen that the shift in flutter q is minor, though

the discrepancy does grow at higher Mach numbers and may become more prevalent for supersonic flows (though this is not explored here). A comparison of the steady Mach field along the wing surface is shown in Fig. 12: the rounded tip has blunted the peak local Mach number at the leading edge (from 1.24 to 1.14), but the flow response outside of this localized area is largely unchanged. This insensitivity may be due to the fact that the wing has no circulation about the wingtip: flutter mechanisms linearized about a lifting flow (a non-zero AoA, e.g.) could be more sensitive to the wingtip geometry.

Viscous comparisons between a flat and a rounded wingtip have not been computed here, but it is likely that the wingtip geometry sensitivity will be even smaller for RANS.

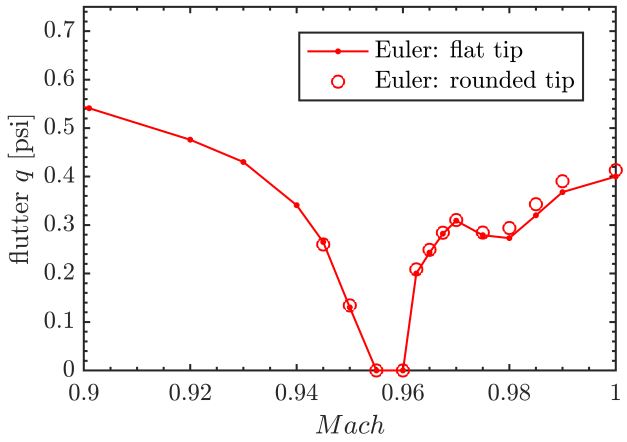

Figure 11: Flutter boundary predicted with inviscid flow, with different wingtip geometries.

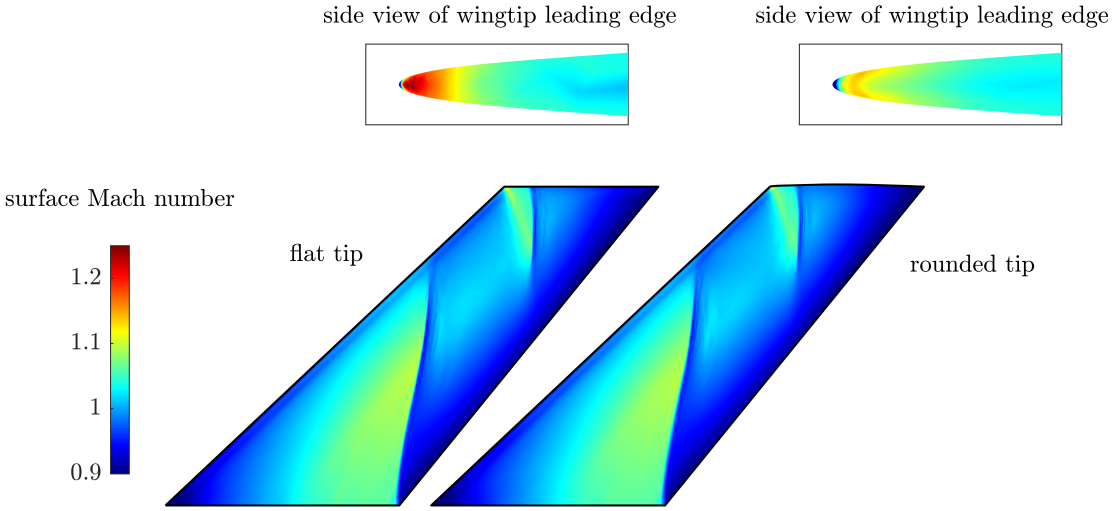

Figure 12: Steady surface Mach numbers computed by the Euler solver when the freestream Mach is 0.96, with different wingtip geometries.

All of the RANS results presented up to this point have utilized a symmetry plane boundary condition at the wing root: the authors are unaware of any literature that does not also utilize this assumption. In reality, of course, the AGARD model was attached to the sidewall of the TDT,[4] and the inboard portion of the wing was immersed in the tunnel's boundary layer. Ref. 28, published contemporaneously with the original AGARD test, quotes a boundary layer thickness for transonic flows at the model mounting location in the 5 - 6 in. range. A more recent reference[29] measures a much larger value of 13 in.: the sizeable discrepancy between these two references is unclear, but either value is nontrivial relative to the 30 in. span of the model. In order to reasonably approximate the impact of this boundary layer, without resorting to a model of the entire TDT test section and plenum (see Ref. 30 for an example of this), a viscous patch

800 in. (flow direction) × 192 in. (vertical direction) was located at the wing root, immersed within a larger symmetry plane boundary of size 1320 in. × 1320 in.

RANS results are obtained for two Mach numbers: 0.9 and 0.96, and the flutter boundary at these two conditions is shown in Fig. 13, where results computed with a symmetric wall are repeated from Fig. 1. Modeling the wall boundary layer at the wing root results in a large increase in flutter q, especially at Mach 0.96, but there is too-little numerical data to know how the shape of the flutter dip has been altered. Crucially, the viscous wall model has degraded the previously-excellent comparison between the prediction and the flutter boundary measured in the TDT, at Mach 0.9. As seen in Fig. 14, however, the confidence in these two new viscous solutions is not as high as seen in previous results, as flutter q is not fully converged with increased mesh density. This is because the mesh refinement process is inclined to add meshing to properly capture the boundary layer growth along the viscous wall, thus detracting from mesh resolution on the wing itself.

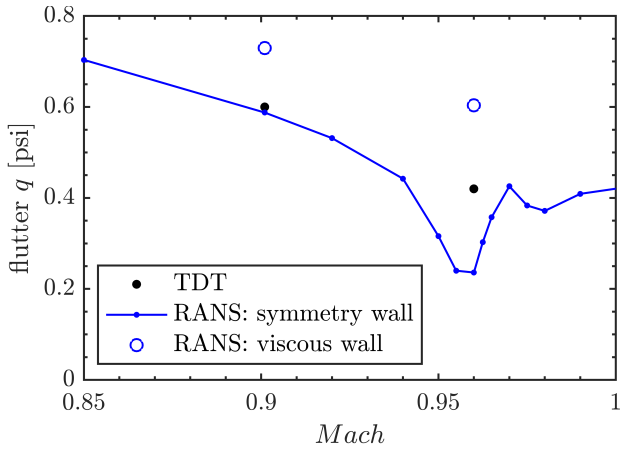

Figure 13: Flutter boundary predicted with viscous flow, for different wall boundary conditions.

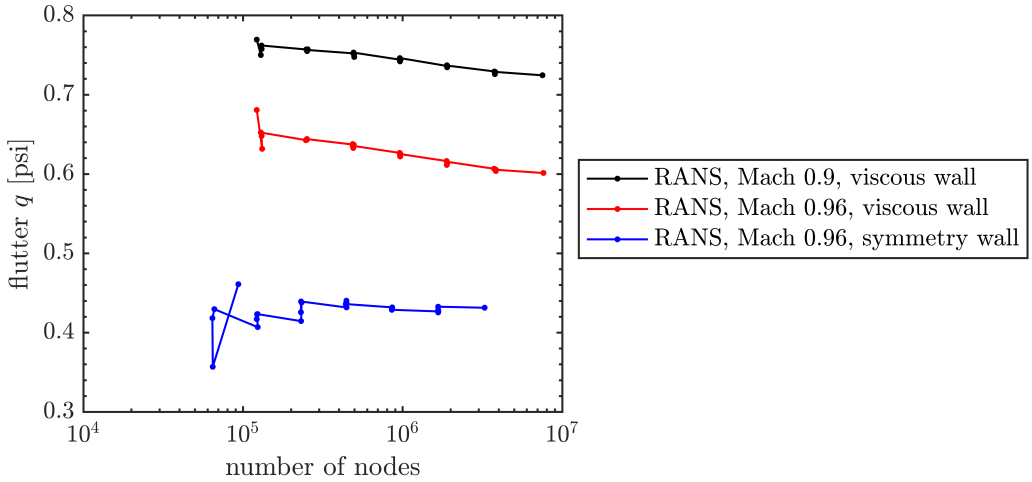

Figure 14: Flutter q convergence during the mesh adaptation process, for different wall boundary conditions.

The boundary layer growth can be seen in Fig. 15 for a Mach number of 0.96. The thickness is nearly 10 in. at the wing leading edge, a value that is greater than the published thickness in Ref. 28, but less than in Ref. 29. The steady surface pressures that result from this viscous flow are shown in Fig. 16, for comparison against previous results (copied from Fig. 6) that utilized a symmetry plane boundary condition at the wing root. As would be expected, the pressure contours at the wing tip are largely unaffected by the altered root boundary condition, but the pressures at the root have a much smaller magnitude, owing to the reduced

local velocity. Most importantly, the shock at the root for Mach 0.96 has disappeared. This reduction in aeroelastic sensitivity is responsible for the increased flutter q in Fig. 13.

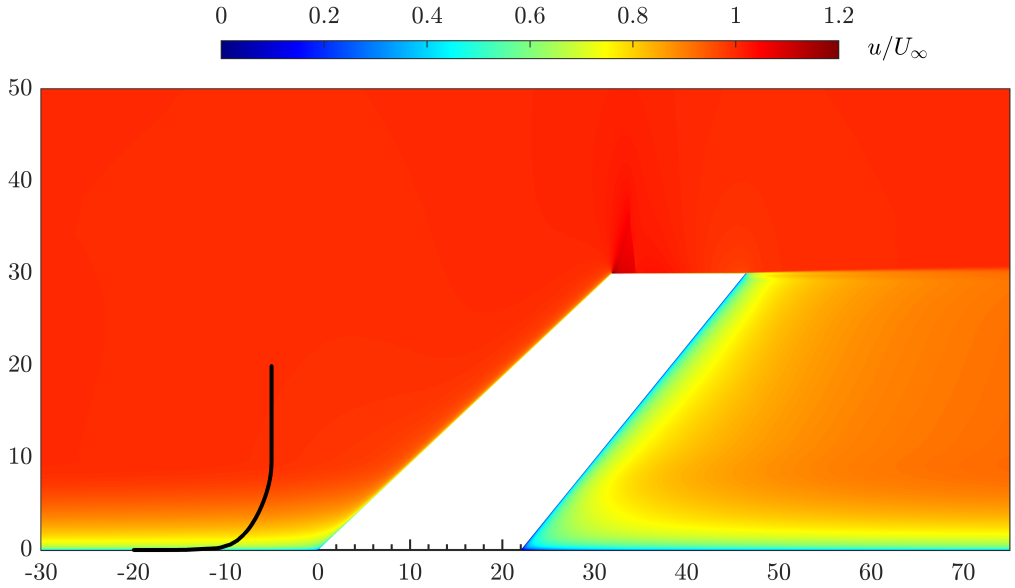

Figure 15: Normalized streamwise flow velocity in the plane of the wing, when the freestream Mach is 0.96.

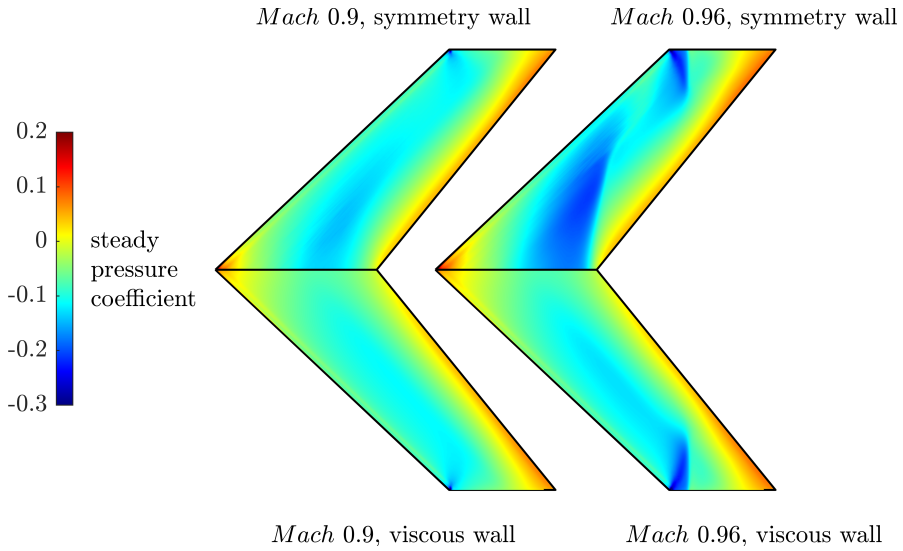

Figure 16: Steady transonic pressure coefficients computed by the RANS solver, for different wall boundary conditions.

V. Future Work

Though the focus of the current paper has been on transonic flutter, this work has also shown large variations in supersonic flutter boundaries for seemingly linear flows, where the sensitivity to model fidelity should be small. One particularly interesting aspect of these flutter mechanisms has been shown in Ref. 15: an inviscid 0-q flutter mechanism in the high supersonic region, via the 3rd vibration mode, at Mach 1.141. The current tools are well-suited to explore this behavior also, and eigenvalue migration results are shown in Fig. 17, which shows the same unstable mode 3 behavior. Mode 3 in this work is a hump mode, which restabilizes at a higher q, whereas Ref. 15 had showed a stronger instability that never restabilized. The

Euler-based flutter q for this Mach is technically 0, as opposed to the value of 2.12 psi shown in Fig. 1, though it is noted that even a small amount of structural damping (which has not been included here), would stabilize this hump mode.

The physics driving this unstable mode 3 behavior, and more generally driving the large sensitivity to fidelity choice in the supersonic regime, will be considered in future efforts.

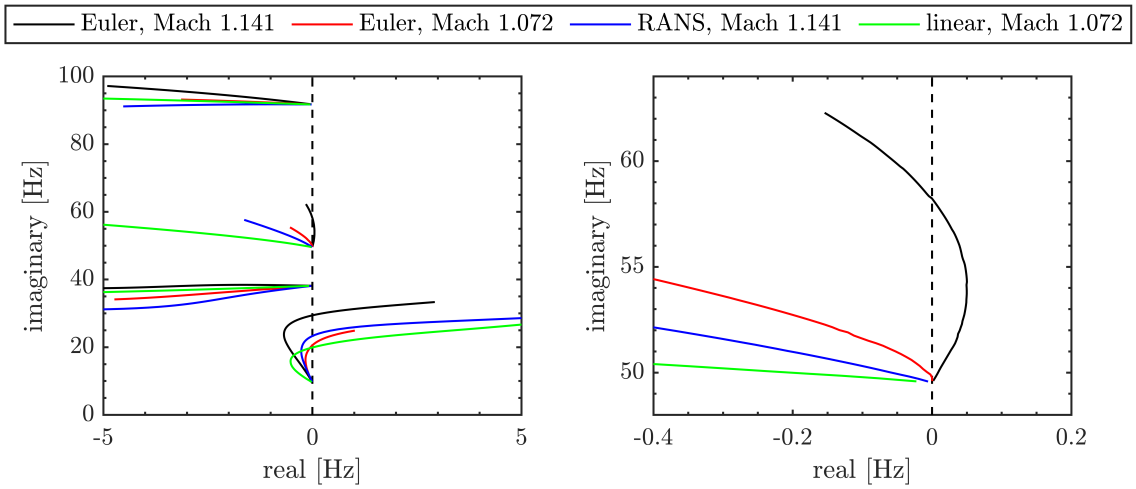

Figure 17: Root locus plots showing the aeroelastic eigenvalue migration. Zoom-in of mode-3 flutter shown on right.

VI. Conclusions

This work has studied the transonic flutter dip of the AGARD 445.6 configuration, a relatively simple aeroelastic configuration tested in the TDT in 1961, and highly referenced by computational aeroelasticians through the present day. This test case is ostensibly used to prove the predictive capability of nonlinear transonic solvers, but the extent of transonic flow for the AGARD wing is unclear, given the small thickness of the symmetric wing, tested at 0° AoA. In this work, to better understand the role of nonlinear transonic aeroelasticity, two numerical tools are used to compute high-quality flutter predictions: a linearized frequency-domain solver implemented within FUN3D/SFE, and the multiscale mesh adaptation scheme from *refine*. The former completely eliminates temporal errors, whereas the latter at least minimizes and quantifies the spatial discretization errors.

With increasing Mach number, weak shocks appear over the wing near Mach 0.9 for Euler solvers, and at a slightly higher Mach number for RANS solvers. Both solvers predict a double flutter dip driven by these flow nonlinearities: the first near Mach 0.96, and the second near Mach 0.98. The severity of this dip inversely correlates with the imaginary part of the GAF term $\bar{A}_{11}$; the extreme case is a positive value of $\bar{A}_{11}$, which drives flutter q to 0 in the first flutter dip predicted by the Euler solver. Both RANS and Euler underpredict the flutter boundary relative to the Mach 0.96 experimental data point (the only data point within the transonic flutter dip region), but there are too-few TDT data points to know if the basic shape and trends of the numerical flutter dips are correct, or not.

Two variants to this baseline case are also considered here: the first swaps out the flat wingtip for a rounded wingtip, as the existing literature is unclear about this detail. For Euler solvers, the flutter boundary is not sensitive to the wingtip geometry, though the peak Mach number at the wingtip is decreased by the rounded tip. The impact on the RANS predictions has not been explored here, though a weak sensitivity is also expected. The second variant attempts to immerse the inboard portion of the model within the boundary layer of the wind tunnel wall. This modeling detail does have a large impact on the flutter boundary (comparisons with TDT data become worse), but the convergence of the mesh refinement tool is not as strong as the cases with a symmetry wall, and furthermore there is some disagreement in the literature regarding the size of the boundary layer in the TDT.

Acknowledgments

This work is supported by the Transformational Tools and Technologies (TTT) project of the NASA Transformative Aeronautics Concepts Program (TACP). Computational resources for this work are provided by the NASA Langley K cluster.

References

[1]Yang, T., Guruswamy, P., Striz, A., Olsen, J., "Flutter Analysis of a NACA 64A006 Airfoil in Small Disturbance Transonic Flow," *Journal of Aircraft*, Vol. 17, No. 4, pp. 225-232, 1980.

[2]Zwaan, R., "Verification of Calculation Methods for Unsteady Airloads in the Prediction of Transonic Flow," *Journal of Aircraft*, Vol. 22, No. 10, pp. 833-839, 1985.

[3]Bendiksen, O., "Review of Unsteady Transonic Aerodynamics: Theory and Applications," *Progress in Aerospace Sciences*, Vol. 47, No. 2, pp. 135-167, 2011.

[4]Yates, C., "AGARD Standard Aeroelastic Configurations for Dynamic Response. Candidate Configuration I - Wing 445.6," NASA TM-100492, August,1987.

[5]Guner, H., Thomas, D., Dimitriadis, G., Terrapon, V., "Unsteady Aerodynamic Modeling Methodology Based on Dynamic Mode Interpolation for Transonic Flutter Calculations," *Journal of Fluids and Structures*, Vol. 84, pp. 218-232, 2019.

[6]Li, H., Ekici, K., "Aeroelastic Modeling of the AGARD 445.6 Wing Using the Harmonic-Balance-Based One-Shot Method," *AIAA Journal*, Vol. 57, No. 11, pp. 4885-4902, 2019.

[7]Pan, J., Liu, F., "Wing Flutter Predictions by a Small-Disturbance Euler method on Body-Fitted Curvilinear Grids," *AIAA Journal*, Vol. 57, No. 11, pp. 4873-4884, 2019.

[8]Rumpfkeil, M., Beran, P., "Multi-Fidelity Surrogate Models for Flutter Database Generation," *Computers and Fluids*, Vol. 197, No. 30, 2020.

[9]Thelen, A., Leifsson, L., Beran, P., "Multifidelity Flutter Prediction using Regression Cokriging with Adaptive Sampling," *Journal of Fluids and Structures*, Vol. 97, 103081, 2020.

[10]Lowe, B., Zingg, "Efficient Flutter Prediction using Reduced-Order Modeling," *AIAA Journal*, Vol. 59, No. 7, pp. 2670-2683, 2021.

[11]Yuan, W., Sandhu, R., Poirel, D., "Fully Coupled Aeroelastic Analysis of Wing Flutter Towards Application to Complex Aircraft Configurations," *Journal of Aerospace Engineering*, 04020117-1, 2021.

[12]Gao, C., Liu, X., Zhang, W., "On the Dispersion Mechanism of the Flutter Boundary of the AGARD 445.6 Wing," *AIAA Journal*, Vol. 59, No. 7, pp. 2657-2669, 2021.

[13]Yates, C., Land, N., Foughner, J., "Measured and Calculated Subsonic and Transonic Flutter Characteristics of a 45-Degree Swept-Back Wing Planform in Air and in Freon-12 in the Langley Transonic Dynamics Tunnel," NASA TN D-1616, 1963

[14]Edwards, J., "Calculated Viscous and Scale Effects on Transonic Aeroelasticity," *Journal of Aircraft*, Vol. 45, No. 6, pp. 1863-1871, 2008.

[15]Silva, W., Chwalowski, P., Boyd, P., "Evaluation of Linear, Inviscid, Viscous, and Reduced-Order Modeling Aeroelastic Solutions of the AGARD 445.6 Wing using Root Locus Analysis," *International Journal of Computational Fluid Dynamics*, Vol. 28, No. 3, pp. 122-139, 2014.

[16]Cunningham, H., Batina, J., Bennett, R., "Modern Wing Flutter Analysis by Computational Fluid Dynamics Methods" *Journal of Aircraft*, Vol. 25, No. 10, pp. 962-968, 1988.

[17]Bartels, R., Rumsey, C., Biedron, R., "CFL3D Version 6.4 - General Usage and Aeroelastic Analysis," NASA TM 2006-214301.

[18]Jacobson, K., Stanford, B., Wood, S., Anderson, W., "Frequency-Domain Flutter Analysis and Sensitivities with Stabilized Finite Elements," *AIAA SciTech Forum*, Orlando, FL, January 6-10, 2020.

[19]Anderson, W., Newman, J., Karman, S., "Stabilized Finite Elements in FUN3D," *Journal of Aircraft*, Vol. 55, No. 2, pp. 696-714, 2017.

[20]Biedron, R., Carlson, J., Derlaga, J., Gnoffo, P., Hammond, D., Jacobson, K., Jones, W., Kleb, B., Lee-Rausch, E., Nielsen, E., Park, M., Rumsey, C., Thomas, J., Thompson, K., Walden, A., Wang, L., Wood, W., "FUN3D Manual: 13.7," NASA TM-2020-5010139.

[21]van Zyl, L., Maserumule, M., "Divergence and the p-k Flutter Equation," *Journal of Aircraft*, Vol. 38, No. 3, pp. 584-586, 2001, https://doi.org/10.2514/2.2805.

[22]Loseille, A., Dervieux, A., Frey, P., Alauzet, F., "Achievement of Global Second Order Mesh Convergence for Discontinuous Flows with Adapted Unstructured Meshes," *AIAA Computational Fluid Dynamics Conference*, Miami, Florida, 2007.

[23]Jacobson, K., Stanford, B., Kiviaho, J., Ozoroski, T., Park, M., Chwalowski, P., "Multiscale Mesh Adaptation for Transonic Aeroelastic Flutter Problems," *AIAA Aviation Forum*, virtual event, 2021.

[24]Kleb, B., Park, M., Wood, W., Bibb, K., Thompson, K., Gomez, R., Tesch, S., "Sketch-to-Solution: An Exploration of Viscous CFD with Automatic Grids," *AIAA Aviation Forum*, Dallas, TX, June 17-21, 2019.

[25]Balan, A., Park, M., Anderson, W., Kamenetskiy, D., Krakos, J., Michal, T., Alauzet, F., "Verification of Anisotropic Mesh Adaptation for RANS Simulations over a ONERA M6 Wing," *AIAA Journal*, Vol. 58, No. 4, pp. 1550-1565, 2020.

[26]Haimes, R., Drela, M., "On the Construction of Aircraft Conceptual Geometry for High-Fidelity Analysis and Design," *AIAA Aerospace Sciences Meeting*, Orlando, FL, January 17-21, 2012.

[27]Spalding, D., "A Single Formula for the "Law of the Wall"," *Journal of Applied Mechanics*, Vol. 28, No. 3, pp. 455-458, 1961.

[28]Staff of the Aeroelasticity Branch "The Langley Transonic Dynamics Tunnel," Langley Working Paper LWP-799, 1969.
[29]Wieseman, C., Bennet, R., "Wall Boundary Layer Measurements for the NASA Langley Transonic Dynamics Tunnel," NASA TM 2007-214867.
[30]Chwalowski, P., Quon, E., Brynildsen, S., "Computational Analysis of the Transonic Dynamics Tunnel using FUN3D," *AIAA SciTech Forum*, San Diego, CA, January 4-8, 2016.